Scientific Research Publishing

Advances in Chemical Engineering and Science, 2023, 13, 172-188
https://www.scirp.org/journal/aces
ISSN Online: 2160-0406
ISSN Print: 2160-0392

A Theoretical Study of Tris-(*o*-benzoquinonediimine)-First-Row Divalent Transition Metal Complexes

Mohammad Abdul Matin[1*], Samiran Bhattacharjee[1], Anwar Hossain[2]

[1]Centre for Advanced Research in Sciences (CARS), Dhaka University, Dhaka, Bangladesh
[2]National University, Gazipur, Bangladesh
Email: *matin123@du.ac.bd

How to cite this paper: Matin, M.A., Bhattacharjee, S. and Hossain, A. (2023) A Theoretical Study of Tris-(*o*-benzoquinonediimine)-First-Row Divalent Transition Metal Complexes. *Advances in Chemical Engineering and Science*, **13**, 172-188.
https://doi.org/10.4236/aces.2023.132013

Received: March 16, 2023
Accepted: April 18, 2023
Published: April 21, 2023

Abstract

The ligand *o*-phenylenediamine (opda) and its oxidized form, *o*-benzoquinonediimine (bqdi), act as a fascinating candidate coordinating toward transition metal ions leading to the photochemical hydrogen production in absence of photosensitizers. Herein, we report the systematic study of the interaction between the oxidized form bqdi ligand, tris-(*o*-benzoquinonediimine) with divalent first-row transition metal series using DFT calculations. The lowest energy structures, bond length, binding energies, frontier molecular orbital analysis, natural bond orbitals, and global reactivity descriptor were calculated using B3LYP/6-311G(d,P) level of theory. The time dependent-DFT at the CAM-B3LYP/6-311+G(d,p) level of theory was applied to determine the electronic structures and the optical spectra. The theoretical binding trend of the divalent first-row transition metal series is decreasing as follows: Cu >Ti > V > Co > Ni > Fe > Cr > Zn >Mn. Among them, the binding potency of iron (II) by the bqdi ligand was not predominantly sturdy as compared to other first-row divalent transition metal ions. The origin of strong coordination with Fe(II) is attributed to its extra capability to induce covalent coordination of bqdi ligands. The complex exhibited two strong peaks at 370 nm and 452 nm, due to the HOMO-3 to LUMO+1 and HOMO-1 to LUMO transitions, respectively. Natural bond orbital analysis showed that the major interaction happens between the N lone pair electrons of the ligand with an anti-bonding orbital of metal ions, in which Ti showed the highest interaction energy than other metal ions. The present systemic DFT study of bqdi ligands with the first-row transition metals strongly encourages the future establishment of photochemical hydrogen production in absence of photosensitizers.

Keywords

DFT, *o*-phenylenediamine, *o*-benzoquinodiimine, First-Row Divalent Transition Metals, Time Dependent–DFT, Coordination Complexes

1. Introduction

This Clean energy production is the ultimate vital problem in the 21st century [1]. The increasing worldwide energy appeal and significant concern about global warming due to the use of fossil fuels have encouraged the development of new technologies and energy carriers [2]. Among the various energy carrier systems, H_2 is the well-known and cleanest energy carrier for the eco-friendly and green environment [3]. Numerous hydrogen production/storage systems, viz., metal/chemical hydrides [4] [5], inorganic and organic nanotubes, [6] and metal-organic frameworks [7], have been reported. In the past decades, non-innocent ligands have been well-known to act as organometallic catalysts and act in the biological framework [8] [9]. The exceptionally abnormal disproportionation reported in non-innocent ligands produces stable oxidizing and reducing agents during the two-electron procedure. For the reduction or oxidation, redox-active ligands have more actively accessible levels [10]. Contrastingly, earlier reports on proton, electron, or hydride shift in functional organic molecules [11] transition-metal complexes with bimolecular, [12] permitted us to unveil the molecular insights of a chemical reaction supported by proton/electron (H^+/e^-) transfer mechanism. These molecular systems might afford an option to extend novel multi-step H^+/e^- movement procedures and hence outcome in the generation of H_2-storage/-evolution materials [13]. Peng *et al.* described the bond patterns of both *o*-benzoquinonediimine (bqdi) and semi-*o*-benzoquinonediimine (s-bqdi) based iron (II), cobalt(II) and cobalt(III) complexes, $[Fe^{II}(bqdi)_3](PF_6)_2$, $[Co^{II}(s\text{-}bqdi)_2]$ and $Co^{III}Cl(s\text{-}bqdi)_2$ [14].

As shown in Scheme 1, the opda ligand coordinated with transition metal ions to produce the corresponding oxidized products, *o*-diiminobenzosemiquinone(sbqdi) and *o*-diiminobenzoquinone(bqdi) through facile oxidation [14]. The free compounds can donate a total of two protons ($2H^+$)

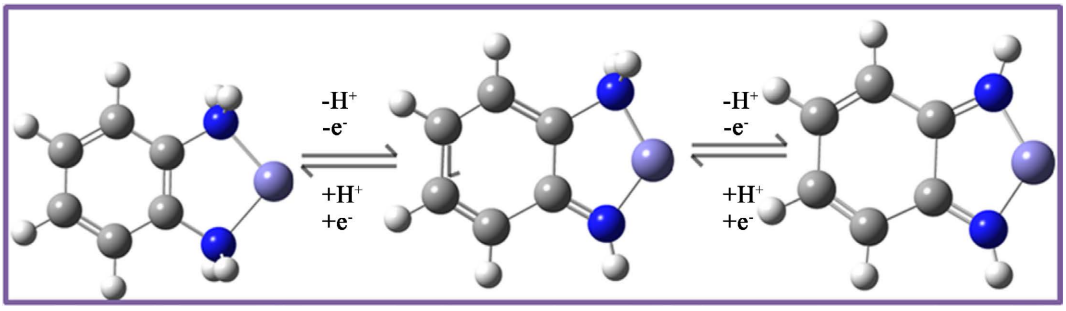

Scheme 1. H^+ and e^- pooling activity of opda complexes. The H, C, and N atoms are illustrated as white, gray, and blue spheres, correspondingly.

and two electrons ($2e^-$) in various combinations. The oxidized form bqdi coordinated with transition metal Fe(II) and formed tris $[Fe(bqdi)_3]^{2+}$ complex. The same groups of researchers also reported the synthesis and crystallographic study of mixed-bpdi-opda ruthenium metal complex, $[Ru^{II}(opda)_2(bqdi)][PF_6]_2$ [15]. They also reported the unsuccessful dissimilar protonation and oxidation states of Ru using metal-assisted ligand oxidation of $[Ru^{II}(opda)(bqdi)_2][PF_6]_2$ to $[Ru(bqdi)_3]^{2+}$. Recently, Matsumoto and co-workers [16] reported the nonprecious-metal-assisted H_2 production from redox active and non-innocent ligand *o*-phenylenediamine (opda) and its Fe(II) complexes. Very recent, they synthesized a low spin (*ls*) iron(II)-bqdi complex, *ls*- $[Fe^{II}(bqdi)_3][PF_6]_2$, displaying photochemical hydrogen evolution(PHE) activity in the THF solvent at room temperature [17]. Such type of metal complexes may uncover functions with energy-related reactions like water splitting, hydrogen production and nitrogen fixation in a chemical process that need multiple proton and electron transfer [18] [19] [20].

However, a systematic study on the first-row divalent transitions series forming tris complexes with bqdi ligand has not yet been reported. Therefore, based on this brief survey, the objective of this study was to investigate the geometries, binding strengths, band gap energy, charges, NBO analysis, and global reactivity descriptors analysis of the 3d transition series forming tris complexes with bqdi ligand $[M(bqdi)_3]^{2+}$ ($[M = Ti^{2+}$ to $Zn^{2+}]$) using density functional theory(DFT) at the B3LYP/6-311G(d,P) level. Specifically, to gain detailed insight into the Fe-bqdi-tris complex, $[Fe(bqdi)_3]^{2+}$, we systematically described the UV and frontier molecular orbitals (FMO).

2. Computational Details

Geometry optimization of the tris(*o*-phenylenediamine) M(II) (where $M = Ti^{2+}$ to Zn^{2+}) complexes were performed in THF using density functional theory (DFT) with the B3LYP/6-311G(d,p) [21] level of theory. The present simulations employed the Gaussian16 simulation package [22] and GaussView 6.0. were applied for the visualization of the optimized geometry. The geometry optimization was considered when the maximal atomic force was smaller than 0.00045 Hartree/Bohr and maximum displacement to threshold value 0.0018 Bohr respectively. No symmetry constraints were imposed for $[M(bqdi)_3]^{2+}$. The effects of solvent were considered by the conductor-like polarizable continuum solvation model (CPCM) [23] [24]. The LANL2DZ effective core potential (ECP) was employed for transition metal atoms and 6-311G(d,p) basis set employed for the other atoms. The lowest energy structures were found by checking normal mode coordinates and without negative frequency. Time-dependent (TD) DFT [25] calculations were executed using the optimized geometry to assess the vertical excitation energies of the equilibrium structures in THF, employing CAM-B3LYP [26]/6-311++G(d,p) level of theory along with long-range corrections. Using the following equation, the coordinated metal-ligand binding energies were calcu-

lated. The equation stated as in Equation (1) [27] [28]:

$$\Delta E = -\frac{E_{complex} - \left(E_{metal} + 3E_{ligand}\right)}{3} \quad (1)$$

where the species $E_{complex}$, E_{metal} and E_{ligand} denotes the energies of $[M(bqdi)_3]^{2+}$ (where M = Ti^{2+} to Zn^{2+}) coordinated complexes, the metal ions and the ligand *o*-benzoquinodiimine(bqdi). Thus, the binding energy, ΔE states for per ligand. Each coordinated complex and ligand was optimized individually. Using NBO 3.1 software that included in the Gaussian program, electronic structures, the natural bond order (NBO), and global descriptors were calculated. For the electronic charges and main donor-acceptor interactions, NBO investigation was executed on the optimized structures. Charges on transition metals were calculated using different charge schemes.

3. Results and Discussions

3.1. Structural Analysis

The geometrical parameters of tris-$[M(bqdi)_3]^{2+}$ (M = Ti-Zn ion) complexes were calculated and summarized in **Table 1**. **Figure 1** shows the optimized structures of the tris(bqdi) transition metal(II) complexes. The optimized geometry of each metal-complex is a distorted octahedron composed of three bidentate bqdi ligands. All the geometries of bqdi ligand-metal complexes are identical as $[Fe(bqdi)_3]^{2+}$ [14], though the metal-Nitrogen(M-N(bqdi)) distances are faintly different (**Table 1**). The metals and nitrogen atoms were 1.960 to 2.270 Å apart on average. The Mn-N bond distances in studied complexes $[Mn(bqdi)_3]^{2+}$ were in the range of 2.270 - 2.273 Å and are quietly longer than the Fe-N distances in $[Fe(bqdi)_3]^{2+}$(1.957 - 1.958 Å). Peng *et al.* [14] reported the bond length of Fe-N in his X-ray geometry analyses of $[Fe(bqdi)_3]^{2+}$ $(PF_6)_2$ complex ranges from 1.906 - 1.925 Å. The average bond length of Fe-N in the tris bqdi complex was found 1.916 Å [29]. Matsmoto *et al.* found the bond distances

Table 1. Structural parameters of the present $[M(bqdi)_3]^{2+}$ coordinated complexes of a variety of metal ions.

Metal	$d_{MN's}$ (Å)	$d_{CN's}$ (Å)	θ_{NMN} (*deg.*)	θ_{CCN} (*deg.*)	θ_{MNC} (*deg.*)
Ti	2.081 (±0.00)	1.32 (±0.00)	91.0 (±11.1)	113.78 (±0.02)	118.54 (±0.04)
V	2.082 (±0.00)	1.30 (±0.00)	90.0 (±10.5)	113.97 (±0.01)	118.16 (±0.01)
Cr	2.042 (±0.04)	1.31 (±0.02)	90.2 (±7.5)	114.59 (±0.14)	116.38 (±1.09)
Mn	2.270 (±0.00)	1.29 (±0.00)	90.6 (±11.5)	116.36 (±0.02)	117.78 (±0.04)
Fe	1.960 (±0.00)	1.30 (±0.00)	90.2 (±6.5)	115.74 (±0.20)	116.99 (±0.07)
Co	2.152 (±0.00)	1.29 (±0.00)	90.2 (±9.7)	115.63 (±0.02)	116.75 (±0.01)
Ni	2.112 (±0.00)	1.29 (±0.00)	90.2 (±8.3)	115.49 (±0.01)	116.17 (±0.02)
Cu	2.173 (±0.19)	1.28 (±0.00)	90.3 (±9.8)	116.23 (±1.04)	116.30 (±5.38)
Zn	2.224 (±0.00)	1.28 (±0.00)	90.5 (±10.2)	116.36 (±0.02)	116.83 (±0.02)

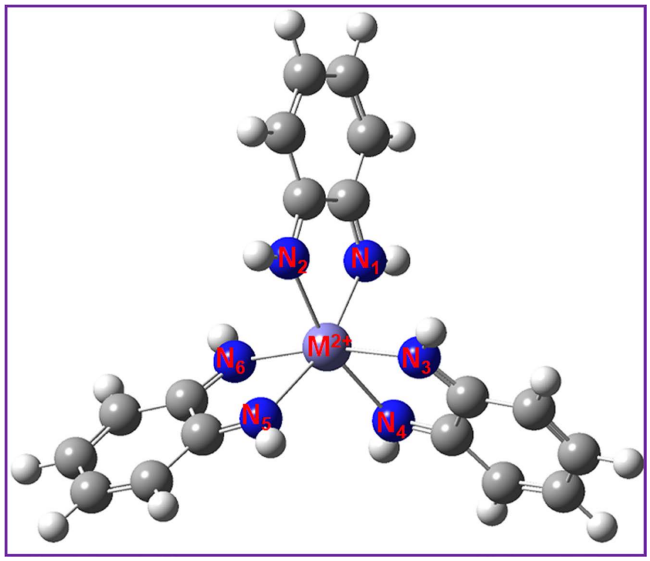

Figure 1. Optimized geometry of the tris-(o-benzoquinonediimine) M^{2+} (where M^{2+} = Ti^{2+} to Zn^{2+}) complex.

of Fe-N ranges from 1.919 - 1.931 Å of the $[Fe(bqdi)_3]^{2+}$ complex [15]. The distances of the M-N in the other tris-*o*-benzoquinonediimine(bqdi) complexes are slightly higher than those of $[Fe(bqdi)_3]^{2+}$, 2.076 - 2.078 Å for $[Ti(bqdi)_3]^{2+}$, 2.075 - 2.076 Å for $[V(bqdi)_3]^{2+}$, 2.003 - 2.085 Å for $[Cr(bqdi)_3]^{2+}$, 2.149 - 2.191 Å for $[Co(bqdi)_3]^{2+}$, 2.047 - 2.416 Å for $[Cu(bqdi)_3]^{2+}$ and 2.219 - 2.221 Å for $[Zn(bqdi)_3]^{2+}$ complexes, respectively. The calculated metal-nitrogen (M-N) distances of these complexes are correlated with the binding strengths of the complexes.

In this work, the calculated N-Fe-N bond angle was predominantly bigger than the preceding X-ray crystal structure, 81.26˚ [14]. Moreover, **Figure 1** also illustrates the trigonally distorted octahedral coordination geometry with the central iron atom. The 'bites' found from *o*-benzoquinonediimine (bqdi) ligands are pronounced and imposed in such a way that the N-Fe-N angles are compacted starting from 90.0˚ to 79.55˚. The extremely tiny Fe-N distances (av. 1.960 Å) specify incredibly strong binding, related iron with low-spin and the bqdi ligand. The geometry of the *o*-benzoquinonediimine(bqdi) ligand is planar. The six C=N bonds (av. l.300 Å) and their six C=C conjugated bonds (av. 1.354 Å) are small, consistent with their recognition as localized double bonds. Kapovsky *et al.* [9] found the calculated C=C bonds of 1.357 Å. The lingering twelve C-C bonds lengths (~1.445 Å) are only faintly smaller than of the C-C single bonds found in cyclooctatetraene (1.46 A). The calculated bonds types of the bqdi ligand in this complex is extremely fastened to those in $[Fe^{II}$-(CN),(bqdi)$]^{2-}$ [29], $[Ru^{II}(bqdi)(bipy)]^{2+}$ [30] and have greatly more localized character than that in $[Ni(s\text{-}bqdi)_2]$ [31].

The bond prototype of the *o*-benzoquinonediimine(bqdi) moiety is also alike in every of the afore mentioned complexes and has additional delocalized double bonds than the neutral or pure *o*-benzoquinonediimine(bqdi) ligand complex.

3.2. Binding Energy Analysis

In this work, we systematically explored the binding energies, ΔE's, enthalpies (ΔH), and Gibbs free energies (ΔG) of the first-row divalent transition metal ions. The binding energies (ΔE), enthalpies, and Gibbs free energies of tris $[M(bqdi)_3]^{2+}$ (where M = Ti-Zn) complexes with different spin states were computed and tabulated in Table 2. The negative binding energies (ΔE) are interrelated with the permanence of the analogous complexes. This explicates that the durability of the complexes in the THF solvent accelerated with the escalating supreme binding energy. Electronic energies are only integrated for the estimation of the above ΔE's binding energies. Since metal-lgand bindings are covalent in nature, hence, the vibrational, thermal, and entropic contributions to ΔE rigged up to be trivial. The calculated binding energies trend is a little bit different due to the stability of the complexes with different spin states. In this study, Fe^{2+} with bqdi ligand-complexes with lower spin is highly stable than other spins of Fe^{2+} [15].

Figure 2 shows double-humped peculiarity in the metal-ligand binding energy versus metals nuclear charges. Because of the increased electronic interaction, on the whole, increases by mounting nuclear charge. Due to Jahn-Teller distortion, the ΔE decreases from V to Cr complexes [32]. The dip in view in favor of Mn was attributed due to the d^5 electronic configuration of Mn(II).The charge transfer from ligand-to-metal is inadequate, due to the occupancy of all d orbitals, resulting in a reduced ΔE. The Zn(II), which has a d^{10} electronic configuration has also shown inefficiency. Hence, this is comparatively little for Zn(II). The double-humped characteristics are alike to that observed for the hexaaqua complexes [33]. Note that the present calculated ΔE's of this study has two peaks located at V and Cu. The two peaks arise due to the high ligand field stabilization in favor of the d^3 and d^9 configuration of high spin complexes.

Following the current ΔE's, Fe(II) is not predominantly strong compared to

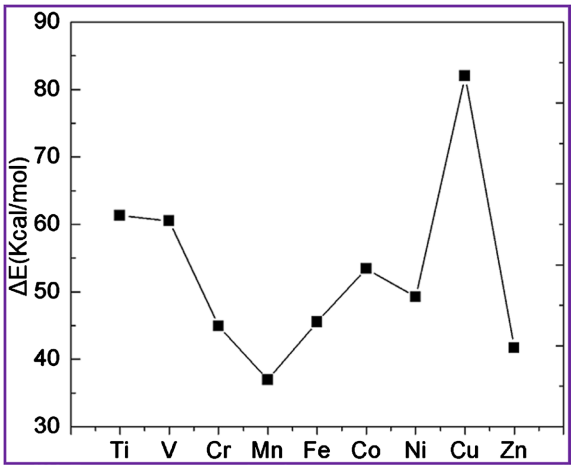

Figure 2. The calculated binding energies of the transition metals coordinated with bqdi ligand. Without imposing the octahedral symmetry, the per ligand binding energy, ΔE was computed for each coordination complex.

other metal ions considered in coordination with the bqdi ligand. Thus, the strong binding of the bqdi ligand examined in presence of Fe(II) should originate from the other factors. The Fe(II) with *ls* (low spin) state is superior to the *hs* state by 3.28 kcal·mol^{-1} (Table 2). Considering the energy, it is screened for the permanence of the complex acceleration in the array of *ls* >*hs*. By evaluating binding energies, it was concluded that Fe(II) at *ls* state was the best choice to form the tris $[Fe(bqdi)_3]^{2+}$ complex. Following the Boys-Bernardi counterpoise (CP) [34] corrected method, it has confirmed the basis set superposition error (BSSE) in support of the tris $[Fe(bqdi)_3]^{2+}$ complex with the low spin state only. The corrected BSSE energy $E_{complex}^{CP}$ (−1148.47 au) was weighed against the uncorrected energy $E_{complex}$ (−1730.06 au). The comparative digression is defined as $\left|\frac{E_{complex}-E_{complex}^{CP}}{E_{complex}}\right|\times 100$.

The calculated BSSE energy was within 0.012% which was the range of computational error.

The electronic energies are only included here to calculate the binding energies. Since the binding of metal-ligand is covalent in nature, the vibrational,

Table 2. The calculated metal-ligand binding energies, enthalpies and Gibbs free energies of the present $[M^{II}(bqdi)_3]^{2+}$ coordinated complexes.

Metal	spin state	ΔE (kcal/mol)	ΔH (kcal/mol)	ΔG (kcal/mol)
Ti	triplet	61.31	61.72	49.19
V	doublet	58.43	59.12	46.11
	quarter	60.54	61.21	48.34
Cr	singlet	44.91	45.33	36.01
	triplet	56.01	56.32	47.51
	quintet	52.53	52.89	44.30
Mn	doublet	39.24	39.12	26.18
	quartet	36.95	37.29	24.77
	sextet	39.53	39.51	28.68
Fe	singlet	51.08	51.76	37.98
	triplet	45.91	46.33	33.54
	quintet	47.80	47.96	36.25
Co	doublet	53.43	53.82	41.02
	quartet	54.58	54.81	42.70
Ni	singlet	49.22	49.49	37.23
	doublet	57.99	58.27	45.96
Cu	doublet	82.03	82.00	70.23
Zn	singlet	41.69	41.75	30.31

thermal and entropic contributions are evicted to be minute. Furthermore, the computed binding enthalpy (ΔH_{bind}) and Gibbs free energy (ΔG_{bind}) of coordination show that the interactions between the ligand bqdi and Fe(II) ion at low spin are higher compared to the high spin and intermediate spin. It is noticed that the complex with the same ligand bqdi low spin complex of Fe(II) is more stable compared to the high spin state. Apart from metal ions, the ZPE-, thermal-energy-, enthalpy-, and Gibbs free energy corrected ΔE's were all indoors 6% of the inaccurate binding energies.

3.3. Spectroscopic Data

The absorption spectrum of the complex $[Fe(bqdi)_3]^{2+}$ was computed using the optimized minimum energy geometry. The calculated UV-Vis absorption spectrum of the complex was illustrated in **Figure 3**. All the calculated wavelengths, oscillatory strengths, and excitation energies of the complex were presented in **Table 3**. In the spectrum, two strong main bands were observed at 370 nm and 452 nm respectively. The maximum absorption band was located at 452.49 nm, supported by the theoretical calculations of Matsumoto *et al.* of the Fe^{2+} complex with bqdi ligand [15]. The theoretical wavelength of the considered structure is supported through the experimentally measured wavelengths at 460 and 635 nm originating as of tris complex of $[Fe^{2+}(Ph2TIP)(tBuDIBQ)]^{2+}$ (4ox), their *o*-diiminobenzoquinone ligand is denoted as DIBQ [35].

The molecular orbitals (MOs) were made known enlarging beginning MO-2 (HOMO-2) to MO+2 (LUMO+2) in **Figure 4** to demonstrate the electronic transitions. The transitions from HOMO-1 to LUMO arose mostly at 452.49 nm. In the HOMO, the density of electrons is mostly disseminated on top of the three bqdi ligands and metal ions but in HOMO-1 mostly covered over the three bqdi ligands. The formation of HOMO-1 orbital is principally owing to 52.78% involvement in the Fe^{2+} iron. The density of electrons has mostly disappeared

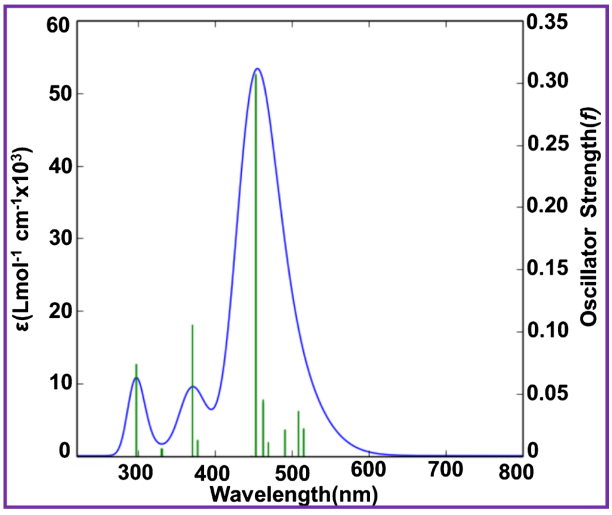

Figure 3. UV-vis absorption spectra of the tris-(*o*-benzoquinonediimine)-Fe^{2+} complex obtained of the present calculation.

Table 3. Vertical excitation energies (in eV), wavelengths (in nm), and oscillator strengths (*f*) of selected transitions for present $[Fe(bqdi)_3]^{2+}$ coordinated complexes in THF obtained by TD-DFT(CAM-B3LYP/6-311++G(d,p)).

Wave length, λ (nm)	E (eV)	Oscillator strength (f)	Major contributions
515.20	2.4065	0.0225	H → L+1 (54%)
515.11	2.4069	0.0220	H → L+2 (54%)
508.71	2.4372	0.0363	H-2 → L+1 (25%), H-1 → L+2 (26%)
490.77	2.5263	0.0213	H-1 → L+1 (14%)
490.66	2.5269	0.0212	H-1 → L+2 (14%), H-2 → L+1 (15%)
469.50	2.6407	0.0111	H → L (60%)
462.47	2.6809	0.0432	H-2 → L (8%)
462.44	2.6811	0.0454	H-1 → L+1 (8%)
452.49	2.7400	0.3070	H-1 → L (55%)
452.29	2.7412	0.3046	H-2 → L (55%)
377.27	3.2863	0.0131	H-3 → L (28%)
370.37	3.3476	0.1058	H-3 → L+1 (31%)
330.56	3.7507	0.0064	H-1 → L+1
298.14	4.1586	0.0741	H-3 → L (32%)
298.04	4.1600	0.0741	H-4 → L (32%)

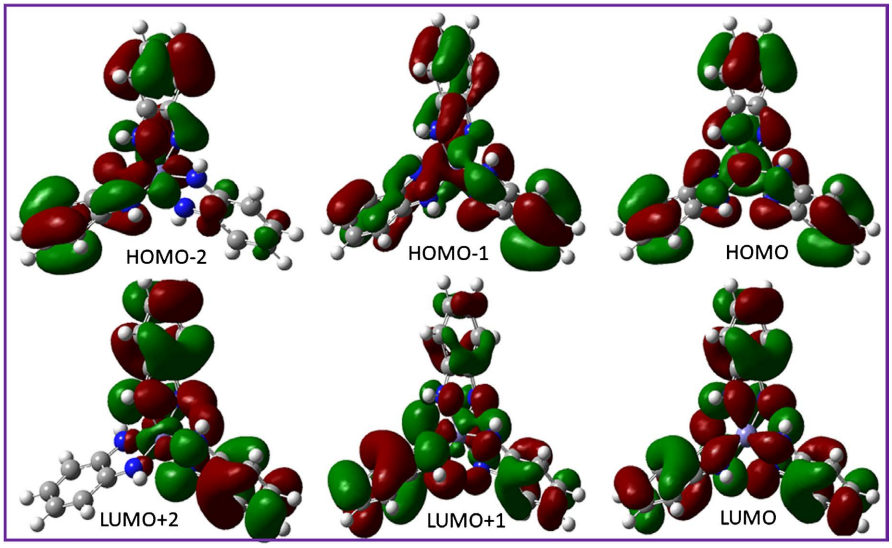

Figure 4. The Frontier MOs of tris-(*o*-benzoquinonediimine)-Fe^{2+} complex. The H, C, and N atoms are illustrated as white, gray, and blue spheres, correspondingly. The orbital lobes presented here in green and red stand for the opposite phases.

from the bqdi ligand from the Fe^{2+} ion in the LUMO orbital presented in Figure 4. Hence, in the UV-vis spectrum, the strongest peak was formed evidently due

to charge transfer from ligand-to-metal (L → M). The orbital LUMO+1 presented here have a similar pattern primary to the major contribution of nitrogen, nearly 52.8% contributions for the construction of LUMO+1 orbital. From Figure 4, it is demonstrated that the HOMO is created from the charge transfer of ligand-to-metal and disported over that three bqdi ligands. The metal ion contributed simply 8.1% electron density during complex formation. The peaks positioned at 370 nm and 452.49 nm arose mostly from the transition from HOMO-3 to LUMO+1 and HOMO-1 to LUMO. The peak located at 452.29 nm arose from the transition of HOMO-2 to LUMO. The HOMO-1 and the HOMO-2 look alike since the electron density is widespread over all the bqdi ligands but reduced a little bit in one ligand. The orbital LUMO+1 is similar to that of the orbital LUMO because the electron density is enclosed surrounding the metal-nitrogen interaction area. The difference between LUMO and LUMO+1 is that LUMO+1 does not have any π character like that of LUMO orbital.

3.4. Atomic Charges

In this study, the charges of metal ions were systematically verified and summarized in Table 4. For the estimation of charges on metal ions, five different charge schemes were applied. The schemes natural population analysis (NPA) [36], Merz-Singh-Kollmann (MK) [37], CHelpG [38], CHelp [39], and HLYGAt [40] were used. The charges on metal ions are assorted from various charge schemes. For example, the charge on Fe at NPA is 1.040, while the charge 0.906 was estimated when the charging scheme MK was applied. Usually, the atomic charges decrease through expanding nuclear charges. The charges on Ti(II) ions with different charge schemes are always higher compared to other metal ions. It is noticed that the charges on Fe(II) ions are not any significant changes with different charge schemes. Regardless, the current trend of atomic charge drifts significantly through homogeneous decline by escalating nuclear charge, found

Table 4. Atomic charges on metals calculated using different charge schemes, NPA, MK, CHelpG, CHelp and HLYGAt.

metal	NPA	MK	CHelp	CHelpG	HYLGAt
Ti	1.041	1.219	1.595	1.531	1.351
V	0.607	1.087	1.378	1.256	1.117
Cr	0.702	0.924	1.233	1.254	1.185
Mn	1.151	0.911	0.972	1.137	0.990
Fe	1.040	0.906	0.963	1.192	1.038
Co	0.933	0.766	0.909	1.016	0.919
Ni	0.823	0.692	0.884	0.946	0.884
Cu	0.876	0.572	0.843	0.851	0.754
Zn	1.255	0.807	0.887	1.123	0.999

in the cross-linking of mussel adhesive proteins [41]. The continuous decrease was ascribed due to the improvement of metal-nitrogen covalent type bond (thus, the improvement of charge relocation from ligand to metal). The geometries studied here, though the calculated atomic charge was found to be a nominal quantity for Cu, despite the charging scheme, and the charge of the atom amplified from time to time by mounting nuclear charge. Such as maximum charge schemes provided an escalating atomic charge starting Cu to Zn.

3.5. NBO Analysis

The natural bond orbitals (NBO) [42] were achieved by applying the NBO 3.1 program executed in Gaussian 16 to compute the energy Eigen values of the frontier molecular orbital ($\Delta E_{\mathrm{LUMO}} - \Delta E_{\mathrm{HOMO}}$) energies. The NBO studies supply information roughly about the electronic structure of a complex. The deviation of a molecule from the Lewis structure was reported by the interactions of occupied and vacant orbitals and hence the pertinent energies can be utilized as a gauge of structural stability.

Using second-order perturbation theory analysis, the donor-acceptor interactions strength is calculated [43]. The second-order perturbation energy, through the delocalization of each donor NBO (i) and acceptor NBO (j) was estimated as follows (Equation (2)).

$$\Delta E_{ij}^{(2)} = -q\frac{\hat{F}_{ij}}{\varepsilon_j - \varepsilon_i} \tag{2}$$

In this equation, q stands for the donor orbital occupancy, ε_i and ε_j are NBO orbital strengths, and $\hat{F}_{ij}$ is the off-diagonal element of the NBO Fock-matrix. The inter-molecular orbital interactions increase with the greater values of interaction energy $E_{ij}^{(2)}$. Thus greater charge transfer occurred among the donors' and acceptors that guided the steadiness of the metal-ligand complex.

The second-order perturbation energies $E_{ij}^{(2)}$ were evaluated and represented the major strong interactions in **Table 5**. The most effective and vital energies

Table 5. Calculated interactions energy E_{ij}^{2} (kcal·mol^{-1}) of the present $[M(bqdi)_3]^{2+}$ coordinated geometries in solution phase at the B3LYP/6-311G(d,p) level of theory.

Donor-acceptor interactions	Ti	V	Cr	Mn	Fe	Co	Ni	Cu	Zn
LP_{N12}-LP^*_M	35.34	50.47	2.68	11.30	16.24	15.60	16.57	18.63	25.54
LP_{N13}-LP^*_M	55.71	35.79	2.67	11.91	16.24	15.56	16.56	18.70	25.50
LP_{N26}-LP^*_M	34.86	50.41	25.63	11.26	15.51	15.59	16.57	20.27	25.54
LP_{N27}-LP^*_M	43.22	38.73	42.97	11.26	14.61	15.60	16.58	11.30	25.56
LP_{N40}-LP^*_M	41.96	39.93	43.11	11.24	14.61	15.59	16.56	11.32	25.54
LP_{N41}-LP^*_M	51.39	37.20	25.31	11.30	15.51	15.61	16.55	20.32	25.51
$\sum E_{ij}^{(2)}$	282.48	252.53	142.37	68.27	92.72	93.55	99.39	100.54	153.19

are linked between the interactions of the lone pair electrons (nitrogen atom) of the ligand (LP_N) and metal anti bonding orbital (LP^*_M). A significant interaction between donor-acceptor specified a higher subsequent value and a pronounced charge transfer through ligand (nitrogen atom) to metal (acceptor). As in Table 5, the computed value for the $[M(bqdi)_3]^{2+}$ complexes decreases from Ti to Mn (282.48 to 68.27 kJ·mol^{-1}) and again increases from Fe to Zn (92.72 - 153.19 kJ·mol^{-1}) respectively. This supports the effective and vital interaction of the bqdi ligand towards metal ions to be exactly the energy investigation. Evaluating the calculated values of ΔE_{bind} (Table 2) and interaction energy (Table 5) illustrate a correlation suggesting the increment of ΔE_{bind} follows the increment of interactions.

3.6. Global Reactivity Descriptors

The information on global reactivity descriptors like band gap (HOMO-LUMO), ionization potential, electron affinity and chemical hardness are very important information for the stability of a complex and are estimated using DFT/B3-LYP/6-311G(d,p) level of theory. Based on band gap energy (HOMO-LUMO), molecules are classified as hard and soft. Due to the small band gap, soft molecules are more polarizable and have a smaller energy of excitation compared to hard one. The HOMO and LUMO energies were used to calculate the ionization potential (I) and electron affinity (A) through the following equations; $I = -E_{\text{HOMO}}$ and $A = -E_{\text{LUMO}}$. Using $\chi = \frac{I + A}{2}$ and $\eta = \frac{I - A}{2}$ equations, electronegativity and chemical hardness are computed. The negative of electronegativity ($\mu = -\chi$) and inverse of hardness, $S = \frac{1}{2\eta}$ were used to calculate the chemical potential and global softness. Global electrophility index ω was derived using the electronic potential, μ and chemical hardness η by the following Equation (3):

$$\omega = \frac{\mu^2}{2\eta} \tag{3}$$

The computed global reactivity descriptors are summarized in Table 6. In these computations tris $[M(bqdi)_3]^{2+}$ complexes of Ti to Zn are considered. The ionization potential and electron affinity is selected as an inverse of HOMO and an inverse of LUMO respectively. The computed ionization potential results of the complexes from $[M(bqdi)_3]^{2+}$ (where M=Ti to Zn) were estimated 8.00, 8.05, 7.16, 7.97, 7.18, 7.92,7.97, 7.92 and 8.00 eV with electron affinity values from 5.44, 5.22, 5.47, 4.82, 5.01, 4.65, 4.65, 4.87 and 4.71 eV respectively. The calculated electronegativity and chemical potential of the studied complexes are 6.72, 6.64, 6.32, 6.40, 6.09, 6.29, 6.31, 6.40 and 6.36 eV from Ti to Zn complexes, respectively. The highest electronegativity values are observed of Ti and V complexes as Ti to Zn complexes the ionization potential increases from Ti to V and increase from Fe to Zn. Moreover, the natural stability and reactivity depends on

Table 6. Global reactivity descriptors of the present $[M(bqdi)_3]^{2+}$ geometries in solution phase(THF) at DFT/B3LYP/6-311G(d,p) level of theory.

Chemical reactivity Indices	Ti	V	Cr	Mn	Fe	Co	Ni	Cu	Zn
E_{HOMO} (eV)	−8.00	−8.05	−7.16	−7.97	−7.18	−7.92	−7.97	−7.92	−8.00
E_{LUMO} (eV)	−5.44	−5.22	−5.47	−4.82	−5.01	−4.65	−4.65	−4.87	−4.71
E_g (eV)	2.56	2.83	1.69	3.15	2.17	3.27	3.32	3.05	3.29
Ionization Potential I (eV)	8.00	8.05	7.16	7.97	7.18	7.92	7.97	7.92	8.00
Electron affinity A (eV)	5.44	5.22	5.47	4.82	5.01	4.65	4.65	4.87	4.71
Electronegativity χ (eV)	6.72	6.64	6.32	6.40	6.09	6.29	6.31	6.40	6.36
Global Hardness (η)	1.28	1.42	0.85	1.58	1.09	1.64	1.66	1.53	1.65
Chemical Potential (μ)	−6.72	−6.64	−6.32	−6.40	−6.09	−6.29	−6.31	−6.40	−6.36
electrophilic indexe (ω)	17.64	15.52	23.50	12.96	17.01	12.06	11.99	13.39	12.26
Global Softness S (eV)	0.39	0.35	0.59	0.31	0.46	0.31	0.30	0.33	0.31

the global softness of the system. The calculated results of the global softness of bqdi ligand with Ti to Zn divalent metal ion complexes are 0.39, 0.35, 0.59, 0.31, 0.46, 0.31, 0.30, 0.33 and 0.31 eV^{-1}, respectively. The low values of global softness as well as the high values of chemical hardness are suggesting the stability of the systems in nature having a minimum reactivity.

Electrophilicity indices of the studied complexes are also estimated at the B3LYP/6-311G(d,p) level of DFT. The computed values of the electrophilic index of these complexes are 17.64, 15.52, 23.50, 12.96, 17.01, 12.06, 11.99, 13.39 and 12.26 eV respectively. Similarly, the higher global hardness and small global softness recommended the systems to be quite stable in nature with minimum reactivity.

On the other hand, electron affinity fluctuates from Ti to Fe and from Fe gradually decreases up to Zn. The decrease in the chemical hardness will lead to an increase in chemical stability of the system. The computed trend of $\Delta E_{HOMO\text{-}LUMO}$ gaps is indicating the chemical stability of the system, *i.e.*; the greater $\Delta E_{HOMO\text{-}LUMO}$ gap furnishes fewer possibilities for electron excitation and makes the structure less reactive. A trend of lessening in the electronic chemical potential of complexes from Ti to Zn is viewed, which increases the stability.

4. Conclusion

The present work theoretically describes the comparative structural properties of first-row divalent transition metal complexes of tris-(*o*-benzoquinonediimine) ligands. The binding strengths, band gap energy, charges, NBO interaction strengths, and global reactivity descriptors analysis were calculated using DFT B3LYP/6-311G(d,P) level of theory. The metal-ligand binding energy is one of the main molecular foundations underlying coordination between metal and bqdi ligands. The present results indicated the most probable way to activate or-

ganic moieties supported with first-row divalent transition metal ions. The present results also suggested that the binding strength of Fe(II) having a low spin state is insufficient to form stable complexes with ligand bqdi. The calculated values were in good agreement with previous experimental results. This result will serve for dynamics of the coordination modeling of such ligand systems in future study.

Acknowledgements

Financial support of this work by the Centre for Advanced Research in Sciences (CARS), University of Dhaka, Dhaka, Bangladesh, is greatly acknowledged.

Conflicts of Interest

The authors declare no conflicts of interest regarding the publication of this paper.

References

[1] Mengele, A.K. and Rau, S. (2023) Learning from Nature's Example: Repair Strategies in Light-Driven Catalysis. *JACS Au*, **3**, 36-46. https://doi.org/10.1021/jacsau.2c00507

[2] Yuan, Y., Liu, X., Tang, W., Li, Z., Huang, G., Zou, H., Yu, R. and Shui, J. (2023) Honeycomb ZrCo Intermetallic for High Performance Hydrogen and Hydrogen Isotope Storage. *Applied Materials & Interfaces*, **15**, 3904-3911. https://doi.org/10.1021/acsami.2c17173

[3] Burton, N.A., Padilla, R.V., Rose, A. and Habibullah, H. (2021) Increasing the Efficiency of Hydrogen Production from Solar Water Electrolysis. *Renewable & Sustainable Energy Reviews*, **135**, Article ID: 110255. https://doi.org/10.1016/j.rser.2020.110255

[4] Brey, J. (2021) Use of hydrogen as a Seasonal Energy Storage System to Manage Renewable Power Development in Spain by 2030. *International Journal of Hydrogen Energy*, **46**, 17447-17457. https://doi.org/10.1016/j.rser.2020.110255

[5] Boateng, E., Zalm, J.V.D. and Chen, A. (2021) Design and Electrochemical Study of Three-Dimensional Expanded Graphite and Reduced Graphene Oxide Nanocomposites Decorated with Pd Nanoparticles for Hydrogen Storage. *Journal of Physical Chemistry C*, **125**, 22970-22981. https://doi.org/10.1021/acs.jpcc.1c06158

[6] Hanif, Z., Choi, K.-I., Jung, J.-H., Pornea, A.G.M., Park, E., Cha, J., Kim, H.-R., Choi, J.-H. and Kim, J. (2023) Dispersion Enhancement of Boron Nitride Nanotubes in a Wide Range of Solvents Using Plant Polyphenol-Based Surface Modification. *Industrial & Engineering Chemistry Research*, **62**, 2662-2670. https://doi.org/10.1021/acs.iecr.2c03897

[7] Bhattacharjee, S., Chen, C. and Ahn, W.S. (2014) Chromium Terephthalate Metal-Organic Framework MIL-101: Synthesis, Functionalization and Applications for Adsorption and Catalysis. *RSC Advances*, **4**, 52500-52525. https://doi.org/10.1039/C4RA11259H

[8] Chirik, P.J. and Wieghardt, K. (2010) Radical Ligands Confer Nobility on Base-Metal Catalysts. *Science*, **327**, 794-795. https://doi.org/10.1126/science.1183281

[9] Kapovsky, M., Christopher, D., Elaine, S.D., Rowshan, A.B., Vanessa, R. and Lever,

A.B.P. (2013) Proton-Induced Disproportionation of a Ruthenium Noninnocent Ligand Complex Yielding a Strong Oxidant and a Strong Reductant. *Inorganic Chemistry*, **52**, 169-181. https://doi.org/10.1021/ic301573c

[10] Naya, S.-I., Kimura, K. and Tada, H. (2013) One-Step Selective Aerobic Oxidation of Amines to Imines by Gold Nanoparticle-Loaded Rutile Titanium(IV) Oxide Plasmon Photocatalyst. *ACS Catalysis*, **3**, 10-13. https://doi.org/10.1021/cs300682d

[11] Costentin, C., Robert, M. and Savéant, J.-M. (2010) Update 1 of: Electrochemical Approach to the Mechanistic Study of Proton-Coupled Electron Transfer. *Chemical Reviews*, **110**, PR1-PR40. https://doi.org/10.1021/cr100038y

[12] Small, Y.A., DuBois, D.L., Fujita, E. and Muckerman, J. (2011) Proton Management as a Design Principle for Hydrogenase-Inspired Catalysts. *Energy & Environmental Science*, **4**, 3008-3020. https://doi.org/10.1039/c1ee01170g

[13] Kuwahara, M., Nishioka, M., Yoshida, M. and Fujita, K.-I. (2018) A Sustainable Method for the Synthesis of Acetic Acid Based on Dehydrogenation of an Ethanol—Water Solution Catalyzed by an Iridium Complex Bearing a Functional Bipyridonate Ligand. *ChemCatChem*, **10**, 3636-3640. https://doi.org/10.1002/cctc.201800680

[14] Peng, S.-M., Chen, C.-T., Liaw, D.-S., Chen, C.-I. and Wanf, Y. (1985) Establishment of the Bond Patterns of *o*-Benzoquinonediimine and Semi-*o*-Benzoquinonediimine: Crystal Structures of Metal Complexes, $[Fe^{II}(bqdi)_3](PF_6)_2$, $[Co^{II}(s\text{-}bqdi)_2]$ and $[Co^{III}Cl(s\text{-}bqdi)_2]$. *Inorganica Chimica Acta*, **101**, L31-L33. https://doi.org/10.1016/S0020-1693(00)87639-2

[15] Cheng, H.-Y. and Peng, S.-M. (1990) Synthesis and Crystal Structure of *o*-Phenylene-Diaminebis (*o*-Benzoquinonediimine) Ruthenium(II) Hexafluorophosphate. *Inorganica Chimica Acta*, **169**, 23-24. https://doi.org/10.1016/S0020-1693(00)82030-7

[16] Matsumoto, T., Chang, H.-C., Wakijaka, M., Ueno, S., Kobayashi, A., Nakayama, A., Taketsugu, T. and Kato, M. (2013) Nonprecious-Metal-Assisted Photochemical Hydrogen Production from *ortho*-Phenylenediamine. *Journal of the American Chemical Society*, **135**, 8646-8654. https://doi.org/10.1021/ja4025116

[17] Matsumoto, T., Yamanoto, R., Wakizaka, M., Nakada, A. and Chang, H.-C. (2020) Molecular Insights into the Ligand-Based Six-Proton- and Six-Electron-Transfer Processes Between Tris-*ortho*-Phenylenediamines and Tris-*ortho*-Benzoquinodiimines. *Chemistry*: *A European Journal*, **26**, 9609-9619. https://doi.org/10.1002/chem.202001873

[18] Verma, P., Weir, J., Mirica, L. and Stack, T.D.P. (2011) Tale of a Twist: Magnetic and Optical Switching in Copper(II) Semiquinone Complexes. *Inorganic Chemistry*, **50**, 9816-9825. https://doi.org/10.1021/ic200958g

[19] Du Bois, D.L. and Bullock, R.M. (2011) Molecular Electrocatalysts for the Oxidation of Hydrogen and the Production of Hydrogen—The Role of Pendant Amines as Proton Relays. *European Journal of Inorganic Chemistry*, **2011**, 1017-1027. https://doi.org/10.1002/ejic.201001081

[20] Bine, F.K., Tasheh, N.S. and Ghogomu, J.N. (2021) A Quantum Chemical Screening of Two Imidazole-Chalcone Hybrid Ligands and Their Pd, Pt and Zn Complexes for Charge Transport and Nonlinear Optical (NLO) Properties: A DFT Study. *Computational Chemistry*, **9**, 215-237. https://doi.org/10.4236/cc.2021.94012

[21] Becke, A.D. (1993) Density-Functional Thermochemistry. III. The Role of Exact Exchange. *Journal of Chemical Physics*, **98**, 5648-5652. https://doi.org/10.1063/1.464913

[22] Frisch, M.J., Trucks, G.W., Schlegel, H.B., Scuseria, G.E., Robb, M.A., Cheeseman,

J.R., *et al.* (2016) Gaussian 16, Revision B.01. Gaussian, Inc., Wallingford.

[23] Barone, V. and Cossi, M. (1998) Quantum Calculation of Molecular Energies and Energy Gradients in Solution by a Conductor Solvent Model. *The Journal of Physical Chemistry A*, **102**, 1995-2001. https://doi.org/10.1021/jp9716997

[24] Cossi, M., Rega, N., Acalmani, G. and Barone, V. (2003) Energies, Structures and Electronic Properties of Molecules in Solution with the C-PCM Solvation Model. *Journal of Computational Chemistry*, **24**, 669-681. https://doi.org/10.1002/jcc.10189

[25] Furche, F. and Burke, K. (2005) Chapter 2 Time-Dependent Density Functional Theoryin Quantum Chemistry. In: David, C.S., Ed. *Annual Reports in Computational Chemistry*, Vol. 1, Elsevier Ltd., New York, 19-30. https://doi.org/10.1016/S1574-1400(05)01002-9

[26] Yanai, T., Tew, D.P. and Handy, N.C. (2004) A New Hybrid Exchange—Correlation Functional Using the Coulomb-Attenuating Method (CAM-B3LYP). *Chemical Physics Letters*, **393**, 51-57. https://doi.org/10.1016/j.cplett.2004.06.011

[27] Matin, M.A., Islam, M.M., Bredow, T. and Aziz, M.A. (2017) The Effects of Oxidation States, Spin States and Solvents on Molecular Structure, Stability and Spectroscopic Properties of Fe-Catechol Complexes: A Theoretical Study. *Advances in Chemical Engineering and Science*, **7**, 137-153. https://doi.org/10.4236/aces.2017.72011

[28] Matin, M.A., Shaikh, M., Hossain, M., Alauddin, M., Debnath, T. and Aziz, M. (2021) The Effects of Oxidation States and Spin States of Chromium Interaction with *Sargassum Sp.*: A Spectroscopic and Density Functional Theoretical Study. *Green and Sustainable Chemistry*, **11**, 125-141. https://doi.org/10.4236/gsc.2021.114011

[29] Christoph, G.G. and Goedken, V.L. (1973) Crystal and Molecular Structure of a Salt of the (o-Benzoquinone Diimine) Tetracyanoiron(II) Ion. *Journal of the American Chemical Society*, **95**, 3869-3875. https://doi.org/10.1021/ja00793a009

[30] Belser, P., Von Zelewsky, A. and Zehnder, M. (1981) Synthesis and Properties of Ruthenium(II) Complexes with o-Quinodiimine Ligands. Crystal and Molecular Structure of Ru(bpy)2(C6H4(NH)2)(PF6)2. *Inorganic Chemistry*, **20**, 3098-3103. https://doi.org/10.1021/ic50223a068

[31] Hall, G.S. and Soderberg, R.H. (1968) Crystal and Molecular Structure of bis(o-Phenylenediamino)nickel, $Ni[C_6H_4(NH)_2]_2$. *Inorganic Chemistry*, **7**, 2300-2303. https://doi.org/10.1021/ic50069a025

[32] Jahn, H.A., Teller, E. and Donnan, F.G. (1937) Stability of Polyatomic Molecules in Degenerate Electronic States-I—Orbital Degeneracy. *Proceedings of the Royal Society of London. Series A*: *Mathematical and Physical Sciences*, **161**, 220-235. https://doi.org/10.1098/rspa.1937.0142

[33] Aakesson, R., Pettersson, L.G.M., Sandstroem, M. and Wahlgren, U. (1994) Ligand Field Effects in the Hydrated Divalent and Trivalent Metal Ions of the First and Second Transition Periods. *Journal of the American Chemical Society*, **116**, 8691-8704. https://doi.org/10.1021/ja00098a032

[34] Boys, S.F. and Bernardi, F. (1970) The Calculation of Small Molecular Interactions by the Differences of Separate Total Energies. Some Procedures with Reduced Errors. *Molecular Physics*, **19**, 553-566. https://doi.org/10.1080/00268977000101561

[35] Bittner, M.M., Lindeman, S.V., Popescu, C.V. and Fiedler, A.T. (2014) Dioxygen Reactivity of Biomimetic Fe(II) Complexes with Noninnocent Catecholate, *o*-Aminophenolate and *o*-Phenylenediamine Ligands. *Inorganic Chemistry*, **53**, 4047-4061. https://doi.org/10.1021/ic403126p

[36] Reed, A., Weinstock, R. and Weinhold, F. (1985) Natural Population Analysis. *The Journal of Chemical Physics*, **83**, 735-746. https://doi.org/10.1063/1.449486

[37] Singh, U.C. and Kollman, P.A. (1984) An Approach to Computing Electrostatic Charges for Molecules. *Journal of Computational Chemistry*, **5**, 129-145. https://doi.org/10.1002/jcc.540050204

[38] Breneman, C.M. and Wiberg, K.B. (1990) Determining Atom-Centered Monopoles from Molecular Electrostatic Potentials. The Need for High Sampling Density in Formamide Conformational Analysis. *Journal of Computational Chemistry*, **11**, 361-373. https://doi.org/10.1002/jcc.540110311

[39] Chirlian, L.E. and Francl, M.M. (1987) Atomic Charges Derived from Electrostatic Potentials: A Detailed Study. *Journal of Computational Chemistry*, **8**, 894-905. https://doi.org/10.1002/jcc.540080616

[40] Hu, H., Lu, Z. and Yang, W. (2007) Fitting Molecular Electrostatic Potentials from Quantum Mechanical Calculations. *Journal of Chemical Theory and Computation*, **3**, 1004-1013. https://doi.org/10.1021/ct600295n

[41] Matin, M.A., Chitumalla, R.K., Lim, M., Gao, X. and Jang, J.K. (2015) Density Functional Theory Study on the Cross-Linking of Mussel Adhesive Proteins. *The Journal of Physical Chemistry B*, **119**, 5496-5504. https://doi.org/10.1021/acs.jpcb.5b01152

[42] Foster, J.P. and Weinhold, F. (1980) Natural Hybrid Orbitals. *Journal of the American Chemical Society*, **102**, 7211-7218. https://doi.org/10.1021/ja00544a007

[43] Reed, A.E., Curtiss, L.A. and Weinhold, F. (1988) Intermolecular Interactions from a Natural Bond Orbital, Donor-Acceptor Viewpoint. *Chemical Reviews*, **88**, 899-926. https://doi.org/10.1021/cr00088a005